Bi-Directional EV Charging With Robust Power Controlled Adaptive Phase-Shift Algorithm

Debasish Mishra , Student Member, IEEE, Bhim Singh , Fellow, IEEE, and Bijaya Ketan Panigrahi , Senior Member, IEEE

Abstract—The charging current variation at various level of battery operating conditions and state of charge (SOC), often requires precise and accurate control in EV charging to achieve desired power transmission. This article proposes a gain adaptive sliding mode control (ASMC) with a modified phase-shift algorithm to facilitate EV fast charging at various levels of non-linear battery dynamics. The ASMC improves the front-end AC-DC charging performance with additional robustness by eliminating the conventional fixed gain control architecture and incorporating dynamic parameter updation at various levels of active or reactive power transmission. In order to support EV fast charging, a modified phase estimation technique is also proposed with an objective to minimize power-mismatch and phase-shift error during bi-directional charging phenomenon. In most of the existing phase-estimation techniques, voltage based PI-controller is used to determine the power transfer limit in bi-directional EV chargers without considering different charging modes and battery SOC. However, the presented control technique is entirely gain adaptive and includes the battery dynamics based upon constant current (CC) or constant voltage (CV) charging phenomenon. The control algorithm is simulated in both grid-to-vehicle (G2V) and vehicleto-grid (V2G) modes of operation to comprehensively analyze the active power exchange without affecting the utility power quality. A laboratory prototype is also developed with a 3.3 kW bi-directional charging topology to validate the controller performances.

Index Terms—Power quality, G2V and V2G bi-directional EV charging, gain adaptive control.

I. INTRODUCTION

THE continuous rise in the adoption of EVs has a tremendous potential to curb greenhouse gas emissions from the transportation sector. EVs are now more frequently considered a wide range of distributed energy in the utility grid [1], [2]. Hence rather than confining the EVs only to uni-directional charging operation, the EV battery storage units are now exposed to bi-directional charging to address various grid power quality issues. Continuous improvements in battery technologies with higher charging cycles, a longer duty of operation, faster charging or discharging rate (C-rate), and higher energy density have made bi-directional charging

Manuscript received 16 January 2023; revised 11 June 2023; accepted 23 June 2023. Date of publication 27 June 2023; date of current version 19 December 2023. This work was supported by SERB-NSC Fellowship. The review of this article was coordinated by Dr. Taner Goktas. (*Corresponding author: Debasish Mishra.*)

The authors are with the Department of Electrical Engineering Indian Institute of Technology Delhi,, New Delhi 110016, India (e-mail: debasish.iitd@gmail.com; bsingh@ee.iitd.ac.in; bkpanigrahi@ee.iitd.ac.in).

Digital Object Identifier 10.1109/TVT.2023.3290116

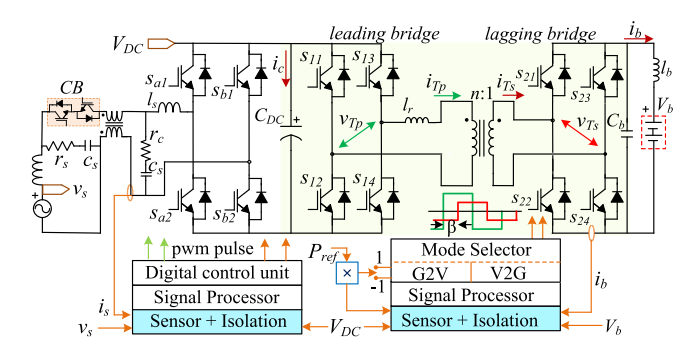


Fig. 1. Circuit configuration for single-phase dual-stage isolated BEV charger.

more attractive [3], [4], [5], [6]. However, the integration of EV clustered networks for large charging establishments, irrespective of the grid non-idealities, has adversely affected the distribution utility. A conventional EV charger without necessary power factor correction (PFC), significantly pollutes the grid by injecting low-order harmonics into it [7], [8]. An enhanced power control algorithm with gain adaptive control architecture is described in this article to ensure bi-directional EV (BEV) charging with improved power quality operation.

Multi-functional EV charging architecture extends its application towards effective utilization of battery energy to overcome various grid power quality issues including the active and reactive power support [9]. However, battery chemistry and associated energy density plays a vital role in determining the extent of utility power support. The batteries with less than 100 Wh/L volumetric energy density and smaller charging rate are least preferred for grid support [10]. Due to higher energy density and increased charging rate, the Li-ion cells are now more preferred for EV battery support. However, converter selection with reduced passive components, galvanic isolation, zero voltage switching (ZVS) and suitable controller design are some of the essential requirements to establish the bi-directional charging. Several well-established works in the literature have demonstrated the application of dual-stage converters as bidirectional EV chargers with enhanced power quality operation and grid strengthening [11], [12], [13], [14], [15].

The BEV charger essentially consists of a two stage of power conversion with independent control architecture for grid connected charging configuration as shown in Fig. 1. Among various control architectures, fixed-gain PWM controllers [16], [17], [18], [19] are mostly adopted in front-end active VSCs

0018-9545 © 2023 IEEE. Personal use is permitted, but republication/redistribution requires IEEE permission. See https://www.ieee.org/publications/rights/index.html for more information.

to maintain a constant DC link voltage with unity power factor (UPF) operation at the utility. Huang et al., have described a PI-control based architecture to regulate the battery voltage from a single-phase utility [17]. However, the cascaded control architecture is highly band-limited within stipulated time-constants across individual control units. Sufficient time constant more than the Nyquist sampling rate, has also been provided for switching pulse generation. Though, the inner-loop bandwidth (BW) is kept quite higher in comparison with the outer voltage loop in [17], the controller is largely affected by time-lag in case of variable load transients. Moreover, the BW of boost converter unit needs to be precisely adjusted in order to limit the effect of RHP zero during reference current tracking [13]. Most of the cascaded PI-control architecture adopts the decoupled current controller to generate the voltage reference vector for active rectifier pulse generation. However, grid-frequency mismatch and error in removal of cross-coupling terms introduces additional inter-harmonics that deteriorate the utility harmonics to a large extent [18]. In [19], PR-controller is implemented to regulate the sinusoidal tracking error more effectively as compared to the dq- controller with elimination of cross-coupling terms. However, the inclusion of parallel resonant blocks to limit each higher-order harmonic disturbances and more sensitive resonant gains [20], adds complexity in the overall control architecture. In addition, the requirement of very high gain at the resonant frequency for complete elimination of multi-harmonic disturbances is quite cumbersome to implement [12]. In order to add more flexibility with active and reactive power variation, direct power control (DPC) algorithm based model predictive control is described in [21]. Although, the predictive control minimizes the tracking error in objective function with variable control weighs, the non-causal signal estimation often introduces large error with variable charging dynamics. The poor voltage regulation at the front-end converter affects the secondary unit of DC-DC converter operation, as the input to the secondary stage expects a least voltage perturbation.

In addition cross-coupled frequency dependent terms aren't also completely eliminated with DPC tracking controller in [21]. Active power decoupling is presented in [22] in order to eliminate the coupling terms to reduce second order power harmonic oscillation. However, introducing a tertiary leg with zero-voltage component injection certainly affects the overall cost and size of the converter. Most of the BEV charging unit comprises of a dual active bridge for the DC-DC power transmission due to its attractive feature on high density power flow and ZVS operation [13]. In order to maintain the UPF operation and EV battery charging regulation simultaneously, the input controller requires a fast regulating action with gain adaptive architecture in lieu of multiple parametric variation and disturbances from either side of controller unit. In [23], a sliding mode control is presented by considering dq-axis current dynamics. Although the stability and controller convergence issues are described thoroughly in [23], the performance indices don't consider the effect of parameter variation during controller implementation and hence the robustness can't be assured at various load operating points.

To address the dual loop voltage and current architecture with parametric disturbance elimination a hysteretic band adjusted SMC design is presented in [24]. However, the gain adaptation and controller convergence with non-linear load operation isn't considered during control law formulation. A number of research works have presented simultaneous control of grid connected converter and secondary stage DC-DC converter. In a double-stage charging architecture, though controllers are entirely decoupled, the interdependency of voltage and current dynamics between both stage converters can't be completely denied, as the primary converter regulates the charging power dynamics of DAB converter. Substantial research works on DAB based EV chargers rely on the phase-shift control between leading and lagging edge full-bridge converters [25], [26]. A current modulation technique is described in [25], with battery current feed-forward for phase-shift control of bridge converter. However, the change in current reference incase high power availability and frequent charging current variation in case of multi-port charging isn't feasible in [25]. A voltage control based phase-shift estimation with a fixed load resistance is presented in [26]. However, the estimation of phase-shift ratio doesn't provide an extended range of operation and limited within a band limited virtual output voltage. Similar studies of independent control technique with dual stage EV charging architecture is also explored in [27]. Although, the fixed gain control architecture regulates each stage dynamics predominantly with enhanced stability, uniform gain can't be applied for each stage of charging dynamics [24].

Citing towards the aforementioned limitations with fixed gain control architecture and band-limited phase-shift control, this article presents an iterative phase-shift control and a gain adaptive sliding mode control for BEV charger operation. The adaptive SMC, as discussed in this article relies on the basic principle of power control theory, which iteratively adjusts the parameter mismatch to add robustness in control implementation. The present control architecture is based on a multi-variable gain adaptation to independently regulate the grid current dynamics during bi-directional charging. In addition to the parameter variation, the controller stability with adaptive gain tuning in presence of grid side disturbance is also analytically proven during controller implementation. The main contributions of this article are highlighted as follows.

- A gain adaptive sliding mode control is implemented in order to enhance the grid power quality with parameter variation and supply disturbances during bi-directional charging.
- Controller stability in presence of external disturbances and convergence are presented analytically with nonlinear stability analysis.
- 3) Phase-shift enhancement is implemented in the secondary stage of the power control algorithm to attribute battery voltage and power mismatch error during EV charging. The equivalent error feed-forward term essentially provides a phase-shift adjustment during battery voltage variation.
- 4) Effect of cross-coupling terms is minimized by including the disturbance limitation in the control algorithm. The experimental analysis is also performed to depict the effect

through significant reduction in low harmonic oscillations with source current harmonic profile.

The rest of the article is presented as follows. A functional analysis related to the overall BEV charging schematic and problem formulation is highlighted in Section II. Detailed modelling, control law formulation and stability analysis for both of the primary and secondary stage converter are described in Section III. Section IV describes the dynamics of controller performances with experimental validation for both of the front-end VSC and DC-DC converter operation.

II. SYSTEM ARCHITECTURE

The grid-interactive BEV charging architecture for a singlephase isolated Level-I charger is shown in Fig. 1. The charging schematic is typically configured with a front-end active bridge converter that regulates the DC link voltage with UPF operation at the utility charging port. A gain adaptive controller with characteristics of parameter adaptation and disturbance rejection is implemented for UPF operation and a fixed DC link operation at C_{dc} . The front-end converter consists of four IGBT switches s_{a1} - s_{a4} that operate with 180° phase opposition to maintain a fixed DC link voltage with input LC filter combination to provide a high impedance path for lower order switching noises. However, to execute the bi-directional charging operation the DC link is controlled at ten percentage higher in magnitude of the source voltage amplitude V_m . The DC-DC power conversion stage is accomplished through a high frequency isolated DAB converter and a series connected inductor l_r to transfer the desired level of charging power in either of the direction. The high voltage side of the DC-DC converter, also known as leading bridge connection operates in similar principle of bridge converter with constant duty and fixed frequency operation. The secondary bridge or lagging bridge of DC-DC converter operates at a variable phase-shift ratio β , to transfer desired level of charging power from either side of the isolated converter. In order to achieve a lower equivalent series resistances (ESR), multiple capacitive units are connected in parallel as output filter of the DAB converter.

Substantial research works have depicted the bi-directional charging operation through the voltage and current PI architecture. However, the battery voltage during CC mode charging doesn't remain constant and the variation is higher with low battery SOC [4]. In order to establish the battery voltage variation in the charging algorithm, an enhanced controller is presented in this article. The modified approach includes the estimation of phase-shift ratio with power and phase mismatch error and represented as,

$$\beta^*(k) = \beta(k-1) + k_p^b(e(k)) + k_i^b T_s(e(k))$$
$$+ f(\Delta P_s(k), \Delta \beta(k))$$
(1)

where e(k), represents the error between the reference and the receiving end power across DAB converter unit. An error minimizing function $f(\Delta P_s(k), \Delta \beta(k))$ is introduced in (1), to take care of the variation of battery voltage during dynamic EV charging. The sequence of controller implementation for BEV charging is presented in Table I.

TABLE I OPERATIONAL SEQUENCE

Sequence of Controller Switching Operation			
	Check the V _{DC} amplitude	Turn-on the front-end	
Step:1	$282V < V_{DC} < 338V$	VSC control unit	
		G2V:Turn-on the leading	
Step:2	Check the power reference	bridge	
	command: G2V or V2G	V2G:Turn-on the lagging	
		bridge	
Step:3	G2V: Check lagging bridge output;	Turn on DAB control at	
_	If $v_{Ts} > V_b$	lagging bridge	
	V2G: Check leading bridge output;	Close the CB and turn-on	
Step:4	If V_{DC} is more than 1.1 times $v_{s(pk.)}$	the DAB control	

III. MODELLING OF FRONT-END CONVERTER

This section presents the decoupled active and reactive power control architecture with a linearized state matrix that includes multiple parameter uncertainies as objective functions. Variable controller gains are evaluated by considering the present and previous values of state vector errors to continusly adjust the controller dynamics. The detailed discussion on system modelling, analysis and control implementaion is described as follows.

A. Control Architecture for Front-End Converter

The state expression for DPC is derived from the fundamentals of stationary-to-rotating axis conversion of utility voltage and current vector as variables with suitable grid frequency estimation. The dq-axis source current expression in a decoupled frame can be written as,

$$\frac{di_d}{dt} = -\frac{r_s}{l_s}i_d + \omega i_q + \frac{v_d - e_d}{l_s} \tag{2}$$

$$\frac{di_q}{dt} = -\frac{r_s}{l_s}i_q - \omega i_d + \frac{v_q - e_q}{l_s} \tag{3}$$

where l_s represents the source side filter inductance and r_s is the equivalent series resistance. The dq-axis components of converter pole voltages are represented by e_d and e_q respectively.

In an ideal single-phase grid connected system, the orthogonal components are obtained through a quadrature delay operation [18], based upon the ADC data acquisition window of the controller and fundamental frequency of source voltage. For instance, a time-base clock (TBCLK) of 100 MHz sampling frequency and data conversion interrupt at 50 kHz switching frequency requires 250 samples for synchronous frame reference generation [28]. However, during peak hour charging and larger non-linear load connectivity with poor power quality condition, the determination of virtual $\alpha\beta$ -components through the conventional sampling delay approach is cumbersome to evaluate and introduces frequency estimation error. The wide range of grid frequency variation, often results in low frequency DC offset introduction to further deteriorate the total harmonic distortions (THD) of input current. In order to improve the estimation process, a second-order generalized integrator (SOGI) [29], is implemented to estimate the $\alpha\beta$ -components and grid fundamental frequency ω . The detailed schematic of grid frequency estimation through SRF-PLL and SOGI algorithm is presented in Fig. 2. To meet the desired charging power transfer limit, a DPC algorithm is implemented in this article with instantaneous

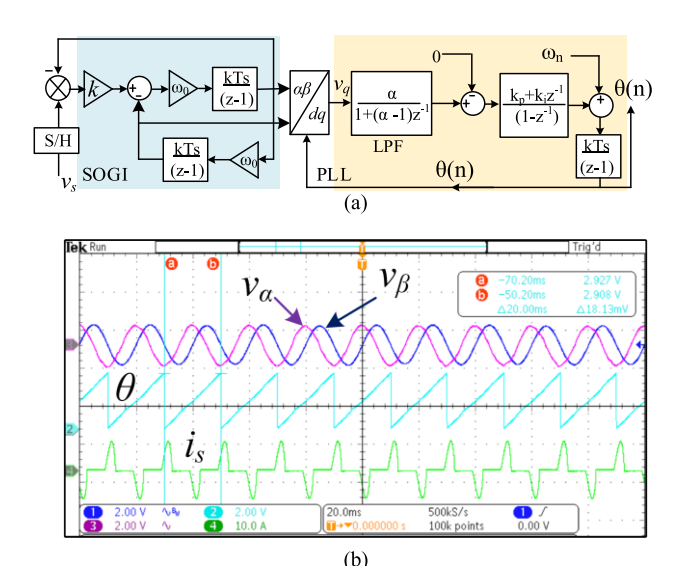


Fig. 2. SOGI filter with (a) control algorithm operation (b) estimation of $\alpha\beta$ -grid voltage components.

reactive power theory (IRPT) [29]. Based on the basics of IRPT algorithm, the active power (P_s) and reactive power (Q_s) for the grid side converter can be represented as,

$$p_s(t) = \frac{1}{2} (i_q(t) \times v_q(t) + i_d(t) \times v_d(t))$$
 (4)

$$q_s(t) = \frac{1}{2} \left(-i_q(t) \times v_d(t) + i_d(t) \times v_q(t) \right)$$
 (5)

Assuming an ideal source voltage with amplitude V_m , the first order time-step derivative of $p_s(t)$ and $q_s(t)$ can be deduced as,

$$\begin{bmatrix} dp_s/dt \\ dq_s/dt \end{bmatrix} = \begin{bmatrix} -\frac{r_s}{l_s} & -\omega \\ \omega & -\frac{r_s}{l_s} \end{bmatrix} \cdot \begin{bmatrix} p_s \\ q_s \end{bmatrix} + \begin{bmatrix} -\frac{V_m}{2l_s} & 0 \\ 0 & -\frac{V_m}{2l_s} \end{bmatrix} \begin{bmatrix} e_d \\ e_q \end{bmatrix} + \begin{bmatrix} \frac{V_m^2}{2l_s} \\ 0 \end{bmatrix}$$
(6)

Redefining the system parameters as $\theta_1(t) = l_s$, $\theta_2(t) = r_s$ and system states as $[x_1(t), x_2(t)]^T = [p_s(t), q_s(t)]^T$, the state matrix in (6) can be written as [20],

$$\dot{x}_1(t) = -\frac{\theta_2}{\theta_1} x_1(t) - \omega x_2(t) + \frac{1}{\theta_1} u_1(t) + d(t) \tag{7}$$

$$\dot{x}_2(t) = -\frac{\theta_2}{\theta_1} x_1(t) + \omega x_1(t) + \frac{1}{\theta_2} u_2(t)$$
 (8)

where $u_1(t) = V_m \ e_d/2$ and $u_2(t) = V_m \ e_q/2$. The state vector $x_i(t) \in R^n$ and control input $u_i(t) \in R^n$ for i = 12. In (7), a uniformly bounded disturbance with upper limit D is considered, where $d(t) \in D$. In order to address the actual scenario during power transmission and to include the parameter uncertainty for additional robustness, the parameter estimation errors are considered in (8) as, $\tilde{\theta}_i(t) = \theta_i - \hat{\theta}_i$, for i = 1 and 2. The controller is designed to generate time variable modulating signal in order to track the reference command input $x_{di}(t)$. To further facilitate the error convergence, during the closed loop error tracking, a sliding surface can be defined as,

$$s_i(x,t) = c_i e_i(x,t), \text{ for } i = 1, 2$$
 (9)

where c_1 is a positive-definite vector. The closed-loop error dynamics can be obtained from (8), can be represented as,

$$\dot{e}_i^T(x,t) = [\dot{x}_i(t) - \dot{x}_{di}(t)]^T \tag{10}$$

To regulate the command tracking with minimal error dynamics, the dq-axis controllers u_1 and u_2 are designed as,

$$-k_1 \operatorname{sgn}(s_1) + \dot{x}_{d1}(t)\hat{\theta}_1$$

$$u_2(t) = -k_{e2}e_2(t) + \hat{\theta}_2 x_2(t) - \omega \hat{\theta}_1 x_1(t) - k_2 \operatorname{sgn}(s_2) + \dot{x}_{d2}(t)\hat{\theta}_1$$

 $u_1(t) = -k_{e1}e_1(t) + \hat{\theta}_2 x_1(t) + \omega \hat{\theta}_1 x_2(t) - d\hat{\theta}_1$

Proof: Considering the system dynamics as defined in (8), a Lyapunov function candidate (LFC) can be chosen as a continuously differentiable function such that,

V(x,t):[0, ∞) $\times D \rightarrow \Re$ is bounded, decrescent that satisfies the expression in [30], for some non-negative constants c_1 and c_2 .

$$c_1(x) \le V(x,t) \le c_2(x)$$
 (12.a)

$$\frac{\partial V}{\partial t} + \frac{\partial V}{\partial x} f(e(t), \tilde{\theta}(t), t) \le 0$$
 (12.b)

Then $V(x,t) \in L_{\infty}$, where L_{∞} represents bounded measurable function in $[0, \infty)$ [30]. Defining the LFC for the system dynamics as described in (8) as,

$$V(x,t) = \frac{1}{2}\theta_1(t)e_1^2(x_1,t) + \frac{1}{2}\theta_2(t)e_2^2(x_2,t) + \frac{1}{\sigma_1}\tilde{\theta}_1(t) + \frac{1}{\sigma_2}\tilde{\theta}_2(t)$$
(13)

The dynamics of the above LFC can be deduced as,

$$\dot{V}(x,t) = -k_{e1,e2} \|e\|_{2}^{2} + \tilde{\theta}_{1} \left(\frac{1}{\sigma_{1}} \dot{\tilde{\theta}}_{1} - \omega e_{1} x_{2}(t) + de_{1} + \omega e_{2} x_{1}(t) \right)$$

$$+\tilde{\theta}_2 \left(\frac{1}{\sigma_2} \dot{\tilde{\theta}}_2 - e_1 x_1(t) - e_2 x_2(t) \right) + \sum_{i=1,2} \left(e_i k_i \operatorname{sgn}(s_i) - e_i \tilde{\theta}_i \dot{x}_{di}(t) \right)$$

$$\tag{14}$$

where the parameter updation law may be defined as,

$$\dot{\hat{\theta}}_1(t) = \sigma_1 \left(\omega e_1 x_2(t) - \omega e_2 x_1(t) - de_1 + e_1 \dot{x}_{d1}(t) \right)
\dot{\hat{\theta}}_2(t) = \sigma_2 \left(e_1 x_1(t) + e_2 x_1(t) + e_2 \dot{x}_{d2}(t) \right)$$
(15)

Substituting the updation law from (15) into (14) results,

$$\dot{V}_i(x,t) = -k_{e1,e2} \|e\|_2^2 + \sum_{i=1,2} e_i k_i \operatorname{sgn}(s_i) - x_{d1}(t) e_1 \tilde{\theta}_1(t)$$
(16)

In (15), the time derivative of q-axis source current command is assumed to be zero to maintain UPF at the grid side. To prove negative semi-definiteness (NSD) of (16) through the conditions as described in (12.a) and (12.b), it is essential to limit the sliding mode constant $k_{1,2}$ with a sufficiently high negative gain. However, in the active power dynamics as in (7), the presence of disturbance term may dominate the other states and hence k_1 is evaluated by limiting the upper bound of source voltage amplitude. The LFC $V_1(x,t)$ from (16) can be rewritten as,

$$\dot{V}_1(x,t) = -k_{e1}e_1^2 - x_1(t)e_1\tilde{\theta}_2(t) - \omega x_2(t)e_1\tilde{\theta}_1(t)$$

$$+e_1k_1\operatorname{sgn}(s_1) - \dot{x}_{d1}(t)e_1\tilde{\theta}_1(t) + de_1\tilde{\theta}_1(t)$$
 (17)

Since the disturbance term is upper bounded as,

$$|d(t)| \le D, \forall t \ge 0 \tag{18}$$

Therefore, (18) can be rewritten as,

$$\dot{V}_1(x,t) \le -k_{e1}e_1^2 - \rho_1 x_2(t) - \rho_2 x_1(t) + k_1 e_1 \operatorname{sgn}(s_1) + De_1 \tilde{\theta}_1(t)$$
(19)

where $\rho_1 = \omega \tilde{\theta}_1 e_1(t)$ and $\rho_2 = \tilde{\theta}_2 e_1(t)$ with an assumption of $\omega x_2(t) > \dot{x}_{d1}(t)$. The limiting constraint in (19) can be written as.

$$\dot{V}_{1}(x,t) \leq -\delta ||x|| - k_{e1}(1-\zeta)e_{1}^{2}(t) - k_{1}\zeta e_{1}^{2}(t)
+ k_{1}|e_{1}(t)| + De_{1}\tilde{\theta}_{1}(t)$$
(20)

where $\delta = \sqrt{(\rho_1^2 + \rho_2^2)}$ and $0 < \zeta < 1$ such that, the inequality in (20) satisfies,

$$|\rho_1 x_1(t) + \rho_2 x_2(t)| \le ||x(t)||_2^2 \sqrt{\rho_1^2 + \rho_2^2}$$
 (21)

To proof the convergence, the expression in (20) must be NSD and the following condition must satisfy,

$$-k_{e1}\zeta |e_1(t)| + k_1 |e_1(t)| + D |e_1(t)| \tilde{\theta}_1(t) \le 0 \tag{22}$$

Similarly keeping the $k_1e_1^2$ fixed, the other constraint from (20) can be derived as,

$$-k_{e1} |e_1(t)| + D |e_1(t)| \tilde{\theta}_1(t) - \beta \zeta ||x|| \le 0$$
 (23)

From (22) and (23) it may be concluded that,

$$k_1 \theta_1 \le k_{e1} \le \beta \zeta. \max(x_1(t), x_2(t)) - D\tilde{\theta}_1$$
 (24)

The constraint for k_{e1} as described in (24), in conjunction with the updation law from (16) essentially satisfies (12.a), (12.b) to proof NSD, hence $V(x, t) \in L_{\infty}$ and subsequently, $e_i(t), x_i(t), \tilde{\theta}(t) \in L_{\infty}$ for i = 1, 2. Since $u_1(t)$ and $u_2(t)$ both are the functions of $e_i(t), x_i(t), \tilde{\theta}(t)$, hence $u_i(t) \in L_{\infty}$ and bounded for i = 12. The switched sliding equivalent control can be proved as a bounded function since,

$$e_i(t)k_{e_i}\operatorname{sgn}(s_i) < k_{e_i}||e_i|| \text{ for } i = 1, 2$$
 (25)

Then it can be shown, the integral of $\dot{V}(x(\tau), \tau)$ results a finite quantity within $[0, \infty)$ and a square-integrable function. Since e(t) is bounded and $e_i(t) \in L_{\infty}$, hence it is uniformly continuous. Then it can be concluded from Barbalat's Lemma [31] that,

$$e_i(t) \to 0, as t \to \infty \text{ for } i = 1, 2$$
 (26)

Hence, the controller is stable and converges to zero as the time approaches a longer duration. The overall control schematic by implementing a sliding controller through direct power control algorithm is shown in Fig. 3.

B. Mathematical Modeling of DC-DC Converter

The DAB topology is widely adapted in most of the Level-1 EV chargers due to it's appealing feature to achieve bidirectional power transfer with galvanic isolation and zero voltage switching (ZVS) with high power transformation capability. The DAB operational modes and corresponding experimental

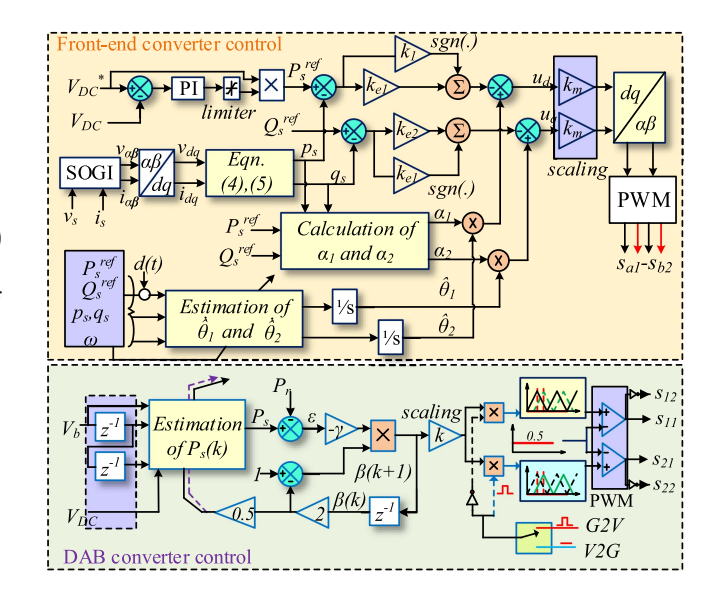


Fig. 3. Control schematic of sliding mode controller during FER operation.

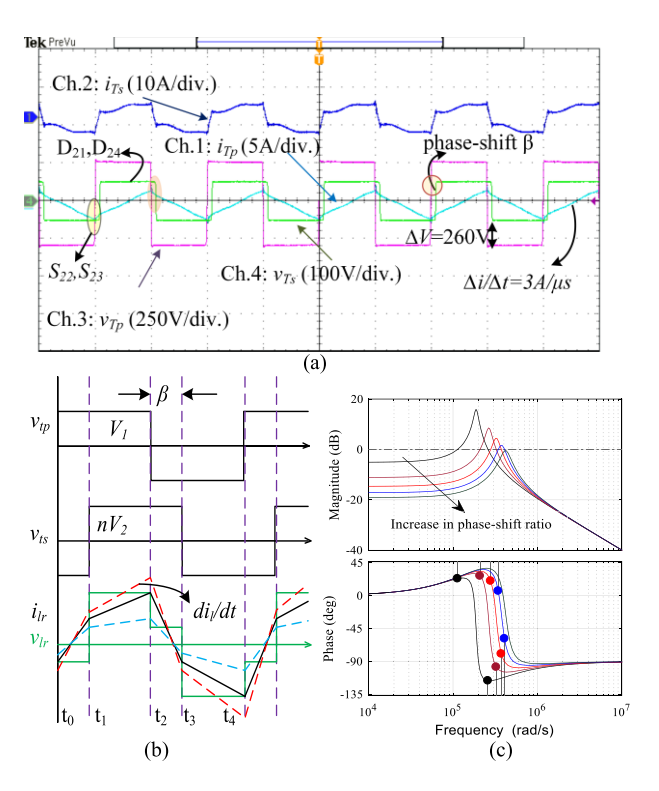


Fig. 4. DAB converter steady-state operation with (a) switching operations (b) HFT dynamics (c) frequency response of state output voltage to input transfer function as in (30).

waveforms are shown in Fig. 4. Considering a symmetrical operation of DAB within half of the switching interval T_{hs} , the current expression at different switching intervals in phase-shifted mode can be derived from Fig. 4(b). The average transferred power during the switching operation T_s , can be calculated as [32].

$$P_{avg.} = \frac{1}{T_{hs}} \int_{0}^{T_{hs}} v_{lr} i_{lr}(t) dt = \frac{nV_{DC}V_{b}}{2f_{sw}l_{r}} \beta (1 - \beta)$$
 (27)

Assuming a continuous conduction mode (CCM), various operating modes of DAB converter can be described as follows.

1) Mode-I (Leading-Edge Discharging Interval): The operational mode starts with the switching operation of s_{11} and s_{14} that induces a square voltage output at the LV side of the transformer with the conduction of s_{22} and s_{23} . Once the interfacing inductor (l_r) completely de-energized, the secondary current reverses its polarity through D_{21} and D_{24} . The state-space equation for the DAB operation in this operational mode can be represented as,

$$\begin{bmatrix} \dot{i}_l \\ \dot{v}_c \end{bmatrix} = \begin{bmatrix} -r_1/l_r & 0 \\ 0 & -1/C_b(R+r_c) \end{bmatrix} \begin{bmatrix} i_l \\ v_c \end{bmatrix} + \begin{bmatrix} 1/l_r \\ 0 \end{bmatrix} V_{DC} \quad (28)$$

where r_1 and r_c represent equivalent series resistances (ESR) associated with l_r and C_b . The states are represented as the inductor (l_r) current i_l and the capacitor (C_b) voltage V_c . The EV battery unit is presented by an equivalent load resistance of R in the state matrix presentation.

2) Mode-II (Leading-Edge Charging Interval): In this mode of operation, due to the leading-edge phase-shift operation the power is transferred from DAB HV side to the EV-battery unit for charging operation as shown in Fig. 4(a). The EV battery starts charging through the free-wheeling diodes D_{21} and D_{24} and the parallel capacitor stores energy for the next switching sub-interval. The variation of current slope with respect to l_r can be observed in Fig. 4(b). The state matrix for this mode of operation is presented as,

$$\begin{bmatrix} \dot{i}_l \\ \dot{v}_c \end{bmatrix} = \begin{bmatrix} -\frac{r_1 + n^2 a r_c}{l_r} & \frac{na}{l_r} \\ -\frac{n(R - a r_c)}{RC_b} & \frac{a}{RC_b} \end{bmatrix} \begin{bmatrix} i_l \\ v_c \end{bmatrix} + \begin{bmatrix} 1/l_r \\ 0 \end{bmatrix} V_{DC}$$
(29)

where $a=R/_{R+r_c}$ and n represents the HFT turn's ratio. Assuming CCM operation of the DAB converter and applying

Assuming CCM operation of the DAB converter and applying state-space averaging technique [29] for a fixed duty cycle and phase-shift ratio β perturbation, the state matrices from (28) and (29) can be averaged as,

$$\begin{bmatrix} \dot{i}_l \\ \dot{v}_c \end{bmatrix} = \begin{bmatrix} -\beta \cdot \frac{r_1 + n^2 a r_c}{l_r} & \frac{na}{l_r} \cdot \beta \\ -\frac{n\beta(R - a r_c)}{RC_b} & -\frac{a}{RC_b} \end{bmatrix} \begin{bmatrix} i_l \\ v_c \end{bmatrix} + \begin{bmatrix} 1/l_r \\ 0 \end{bmatrix} V_{DC}$$
(30)

The steady-state solution from (30) leads to the following state-to-input transfer function matrix:

$$\begin{bmatrix} i_{l}(s) \\ v_{c}(s) \end{bmatrix} = \begin{bmatrix} \frac{(RC_{b}s+a).V_{DC}(s)}{RLC_{b}s^{2} + \beta(r_{1}RC_{b} + n^{2}ar_{c}RC_{b} + al_{r})s + a(r_{1} + n^{2}R)\beta} \\ \frac{\beta(nR - anr_{c}).V_{DC}(s)}{RLC_{b}s^{2} + \beta(r_{1}RC_{b} + n^{2}ar_{c}RC_{b} + al_{r})s + a(r_{1} + n^{2}R)\beta} \end{bmatrix}$$
(31

The frequency response of the above control to state output transfer function is shown in Fig. 4(c). It may be observed that, though the system transfer function depicts a stable frequency response, the increase in phase-margin at higher phase-shift ratio limits the transient performance during high power transmission. The fixed gain controllers as in the conventional voltage or current mode technique thus imposes restriction for choosing controller gains during high power charging requirements [27]. Hence a modified phase-estimation technique is essential to determine the phase-shift ratio, by considering additional phase-shift ratio to eliminate power mismatch error.

C. Enhanced Phase-Shift Algorithm for DAB Converter

The phase-shift variation is one of the fundamental techniques for bi-directional power transmission across DAB power converters. Based upon the similar principle of power transmission across an over-head transmission line, the phase estimation technique considers both sending and receiving-end voltage to determine the level of active power transmission. However, during the charging of a dip discharged EV battery, although the DC link voltage remains constant, the battery voltage dynamics follows a non-linear charging path. Hence, the linear calculation of power variation can't be established during EV battery charging [26]. In order to enhance the charging dynamics and power transmission characteristics, this article introduces an iterative phase-shift estimation based upon gradient-descent algorithms. The gradient descent algorithm minimizes an error function through negative gradient of an objective function to obtain the local minima. Hence, the estimation architecture is computationally efficient that can be implemented through a digital processor within less converging time [33]. The proposed algorithm includes the power reference error and battery voltage mismatch as two objective functions to determine the phase-shift ratio (β). Considering a quadratic cost function as,

$$J(\beta) = \frac{1}{2} [P_s(t) - P_{ref}]^2$$
 (32)

where $P_s(t)$ is the sending-end power as given in (27), and P_{ref} is the desired reference power for EV charging.

In case of ideal battery charging or higher value of SOC, the battery voltage V_b doesn't vary to a large extent. However, due to the nonlinearity in EV charging, the error appears between the reference power and actual sending-end power. Minimizing the error, through the negative gradient of the cost function as in (32), the phase-mismatch error can be evaluated as [33],

$$\frac{\partial \beta}{\partial t} = -\gamma \varepsilon_p \frac{\partial \varepsilon_p}{\partial \beta} \tag{33}$$

where γ , is the convergence factor that can be varied within 0.2 to 0.5 based upon the need of convergence rate and ε_p represents the power mismatch error in (32). The dynamics of the first order time variation of the power deviation error can be found out from (27), which is represented as,

$$\frac{\partial \varepsilon_p}{\partial \beta} = \frac{nV_{DC}V_b}{2f_{sw}l_r} \left(1 - 2\beta\right) \tag{34}$$

Substituting the expression of (34), in (33), the phase-shift ratio can be represented as,

$$\frac{\partial \beta}{\partial t} = -\gamma \varepsilon_p \frac{nV_{DC}V_b}{2f_{sw}l_r} \left(1 - 2\beta\right) \tag{35}$$

Discretizing the above expression in (35), the phase-shift ratio β , may be expressed as,

$$\beta(k+1) = -\gamma \varepsilon_p \frac{nV_{DC}V_b(k+1)}{2f_{sw}l_r} \left(1 - 2\beta(k)\right)$$
 (36)

However, the above expression requires a step ahead estimation of battery voltage, which can be obtained from Lagrange's

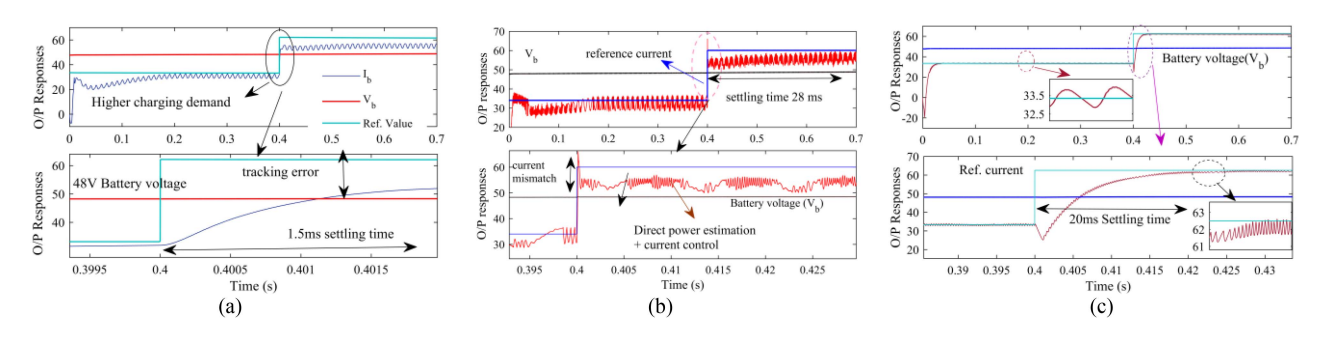


Fig. 5. Simulation waveforms representing the dynamic responses of battery unit with (a) voltage control technique [25](b) current control technique [26] and (c) proposed modified phase-shift algorithm.

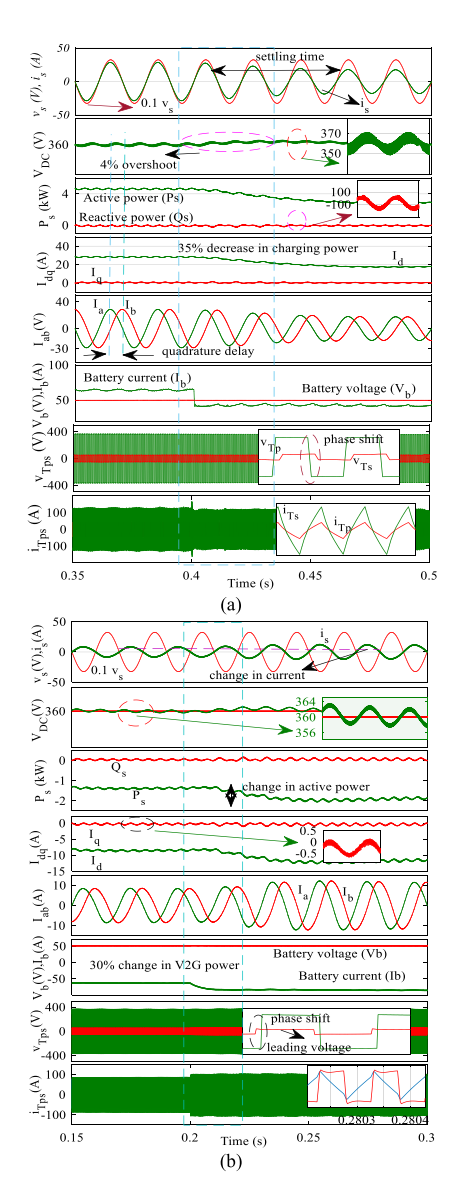


Fig. 6. Charging performances with (a) G2V and (b) V2G dynamics.

extrapolation method and represented as,

$$V_b(k+1) = 3V_b(k) - 3V_b(k-1) + V_b(k-2)$$
(37)

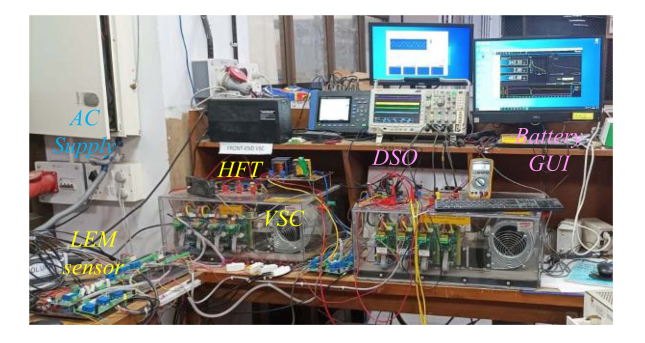


Fig. 7. Experimental prototype of bi-directional EV charging architecture.

The phase-shift estimation as in (36), includes the time-variation of battery voltage dynamics, to effectively incorporate the charging non-linearity during reference power tracking. The estimation of β , expects a continuous adjustment with unit sample delay to minimize the power mismatch error. The weighing factor γ , plays a crucial role in determining the rate of convergence during reference power tracking. Hence, to evaluate γ , the averaged dynamics of phase-shift ratio is considered at the maximum operating point, which is presented as,

$$\frac{\partial \beta_{av}}{\partial t} = -\gamma \cdot \frac{2}{T_s} \int_{t_0}^{t_o + T_s/2} \frac{n\varepsilon_p V_{DC} V_b}{2f_{sw} l_r} (1 - 2\beta) dt \qquad (38)$$

Applying the principle of change in variables with the integral limits, it may be written as,

$$\frac{\partial \beta_{av}}{\partial t} = -\gamma \frac{n\varepsilon_p V_{DC} V_b}{2f_{sw} l_r} \beta \left(1 - \beta\right) \tag{39}$$

From the above expression of averaged value of phase-shift ratio β_{av} and the equilibrium point, the weighing factor γ can be evaluated as,

$$\gamma = \frac{2f_{sw}l_r}{n\varepsilon_p V_{DC}V_b (1 - \beta_m)} = \frac{4f_{sw}l_r}{n\varepsilon_p V_{DC}V_b}$$
(40)

Based on the conventional phase-shift algorithm [23] and the phase-error as in (36), the combined expression for modified phase-shift ratio can be derived as,

$$\beta^{*}(k+1) = \frac{\frac{1}{2} - \sqrt{\frac{1}{4} - \frac{2f_{s}l_{r}P_{s}}{nV_{DC}V_{b}}} + \hat{\beta}(k+1), for \text{ leading edge}}{-\frac{1}{2} + \sqrt{\frac{1}{4} - \frac{2f_{s}l_{r}P_{s}}{nV_{DC}V_{b}}} - \hat{\beta}(k+1), for \text{ lagging edge}}}$$
(41)

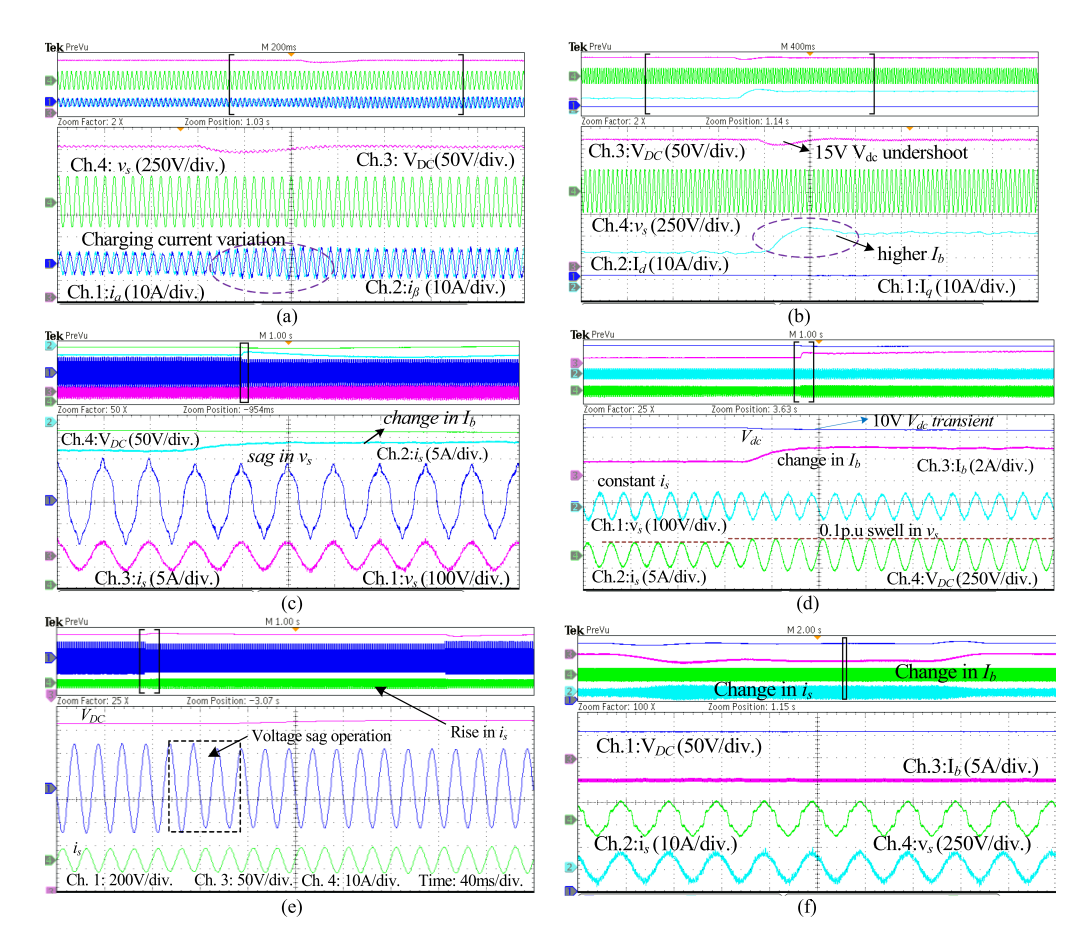


Fig. 8. Experimental results for (a) G2V operation (b) charging current variation with UPF operation (c) responses of G2V battery voltage and current dynamics (d) responses with higher charging current (e) V2G voltage and current dynamics (f) BEV charger responses with disturbance rejection.

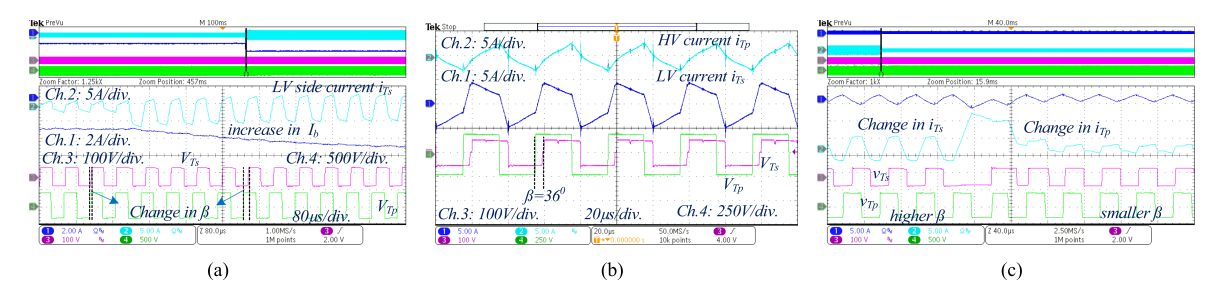


Fig. 9. Dynamics of DAB converter with (a) higher charging operation (b) high-frequency transformer dynamics (c) reduced charging operation.

The expression in (41) has two terms explicitly defining the operating phase-shift ratio with respect to maximum ratio of 0.5 and an additional phase-shift error to address power mismatch.

IV. RESULTS AND DISCUSSION

The bi-directional EV charging architecture is designed in MATLAB simulation with a 48 V EV battery and 4 kVA high-frequency transformer (HFT). The detailed system and control parameters are described in Table II. The simulated voltage and current characteristics of BEV charging, are shown in Fig. 5 to describe a comparative analysis of various phase-shifting algorithm. Fig. 5(a) and (b) depicts the simulation results with conventional voltage and current control techniques [25], [26]. The tracking performance with modified phase-estimation

TABLE II
SYSTEM AND CONTROL PARAMETERS

System	Value	Control	Value
Parameters		Parameters	
v_s	230V/50Hz	k_{e1} , k_{e2}	0.01,5e-4
r_c, c_s	100Ω, 2μF	k_1, k_2	0.1, 0.05
C_{dc}	2700μF	k_p, k_i	0.25, 0.7
C_b , l_b	540μF,400μΗ	γ	0.015
EV battery	48V, 100Ah	$f_s(DAB)$,	25kHz,
		$f_s(VSC)$	7.5kHz
HFT $l_p:l_s$	18µН: 6μН	l_r	27μΗ

is shown in Fig. 5(c), to describe the improvement in tracking time and ripple current magnitude as compared to conventional methods. The simulated results of charging power variation, through the BEV charger with active front-end converter are

shown in Fig. 6. The active power exchange in G2V charging mode of operation for a maximum of 4.1 kW is shown in Fig. 6(a). To verify the controller performance, a lower step charging command is provided at 0.41 sec., which is reflected at each step voltage and current dynamics. The front-end controller maintains UPF operation throughout the G2V and V2G mode of operation. Fig. 6(b) shows the V2G mode of operation, where the source voltage and current are 180° phase apart. The minimal DC link voltage ripple contents during charging power dynamics, ensures the reliability of controller implementation. The experimental setup for the single phase EV charging architecture is shown in Fig. 7.

A. Performances of Front-End Converter Dynamics

The dynamic responses of grid side converter during G2V mode operation are shown in Fig. 8(a) and (b), where UPF operation can be seen with minimal DC under-shoot. The charging current variation during G2V mode of operation with unity power factor operation can be clearly inferred from Fig. 8(b), where the q-axis source current is maintained at zero. The charging current variation in presence of distorted grid condition is shown in Fig. 8(c) and (d) with 5 V of DC link voltage ripple at double frequency oscillations. Fig. 8(e) describes the V2G operation, with voltage sag and swell operation. During the source voltage variation the input current i_s adjusts itself to maintain the DC link voltage. The source voltage and current are phase-opposite to each other during V2G dynamics with a fixed DC link operation. The intermediate DC bus voltage is shown with 50 V/div. to identify the voltage variation during discharging dynamics. Similar experimental conditions are also created to evaluate the charging performances during distorted supply voltage input as shown in Fig. 8(f). The voltage distortion is obtained by adding 0.05 p.u lower order harmonic voltages with the fundamental input voltage through a grid simulator. The dynamic performance depicts a sinusoidal current following nature of the EV charger with minimal DC link variations.

B. Performances of DC-DC Converter Operation

The single phase-shift (SPS) modulation technique is implemented to experimental obtain the power variation across DAB converter. The charging current variation of 2.5 A is shown in Fig. 9(a) with change in phase-shift control that can be clearly identified from a higher phase-shift ratio β . The high frequency transformer current and voltage dynamics are shown in Fig. 9(b). The zero voltage switching operation at a phase-shift ratio $\beta =$ 36° is shown in Fig. 9(b). The high voltage and low voltage side currents i_{Tp} and i_{Ts} varies according to the required charging current demand with the estimated phase-shift ratio. The change in voltage and current dynamics with lower charging current demand or equivalent constant voltage operation is shown in Fig. 9(c). During the immediate change in charging current demand a current overshot can be observed at the LV side of the high frequency transformer. However, the overshoot is limited only to a single cycle delay operation to avoid any interlayer insulation damages. Both of charging operation in Fig. 9(a) and

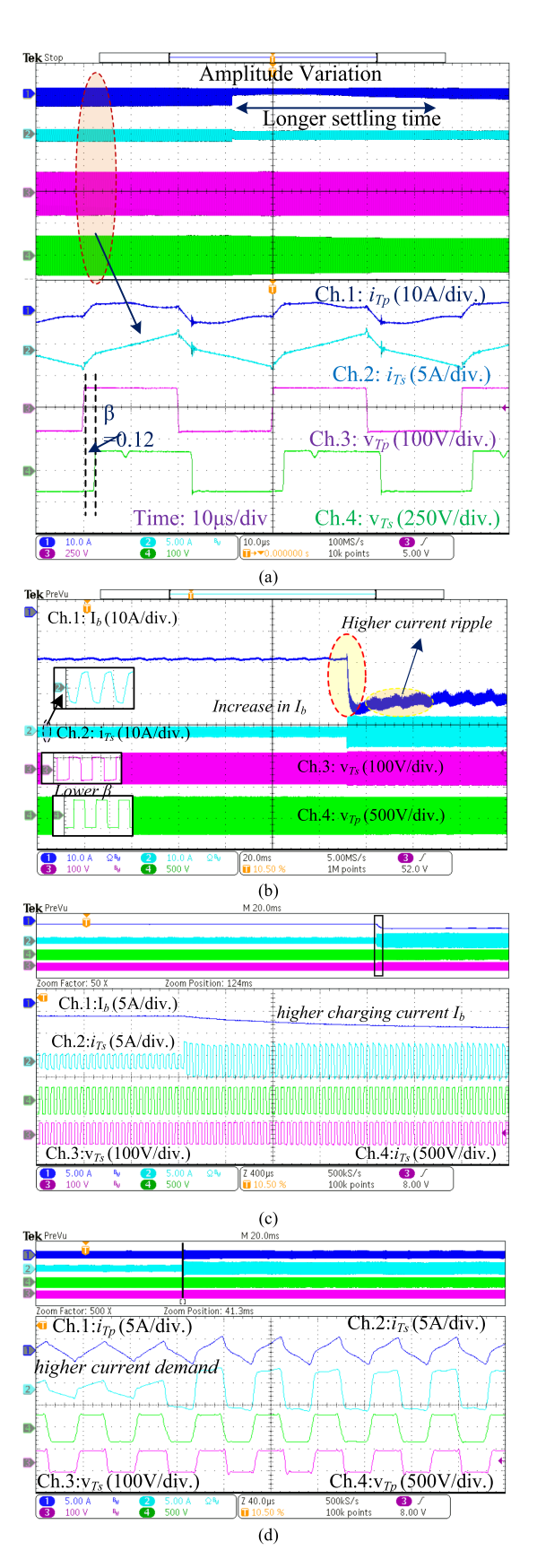


Fig. 10. The DAB performances during (a), (b) higher current demand with (SPS) modulation (c), (d) enhanced phase-shift algorithm.

(b) are operated at 25 kHz switching frequency at fixed duty and variable phase-shift operational modes.

C. Comparative Analysis of Phase-Shift Enhancement

The experimental performances of conventional single phase modulation (SPS) algorithm is compared with the modified phase-shift algorithm by considering reference charging current variation for a nearly discharged battery. A change in current command produces a significant battery voltage variation, which requires an immediate deflection in phase-shift control parameter. The modified phase-shift control provides an immediate feed-forward phase control that combines with the calculated β angle to track the reference command as described in (41). The dynamics of charging performances can be observed as shown in Fig. 10(a) and (b). The conventional control algorithm tracks the reference charging demand through battery current I_b oscillation and longer settling time. However, significant improvement can be observed in Fig. 10(c) and (d) where a quick settling improvises the charging dynamics with the enhanced phase-shift algorithm. The higher charging current command is settled within few cycles of transformer secondary current magnitude. The battery current smoothly achieves the desired dynamics with enhanced phase control algorithm. After achieving the charging current dynamics, the feed forward phase term reduces to zero and the SPS current control follows the charging dynamics.

V. CONCLUSION

An adaptive sliding mode control based bi-directional EV charging topology is exclusively discussed with controller stability and convergence for primary stage rectification. The experimental results validate the implementation of the adaptive SMC, to achieve an improved charging profile during charging operation. The adaptive SMC algorithm evaluates a variable controller gain at each sampling step of data acquisition to establish the desired power reference command that suitably nullifies the effect of uncertainties at input voltage distortions. In addition, an enhanced phase-shift algorithm is implemented to effectively control the DC charging dynamics with minimal phase delay operation. The iterative phase-shift estimation evaluates the power mismatch error at each switching interval and provides an equivalent feed-forward phase-shift error ratio to enhance the dynamics of charging operation. The modified algorithm incorporates the change in battery voltage dynamics to provide a robust phase-shift estimation for DAB charging operation. The present control algorithm is widely adaptable for a large charging current variation in a deeply discharged battery charging operation. The charging robustness and experimental performances depicts its appealing feature in bi-directional EV charging applications.

ACKNOWLEDGMENT

The authors are grateful to SERB-NSC Fellowship and DRIIV, an initiative of the Principal Scientific Advisor (PSA), Delhi S&T Cluster, Government of India for supporting this work.

REFERENCES

- [1] Z. Wang, X. Guo, J. Li, and X. Wang, "Impact of voltage sags on electric-vehicle charger and critical voltage sag determination," *IEEE Trans. Power Del.*, vol. 31, no. 16, pp. 1397–1399, Jun. 2016.
- [2] Y. Yuan, L. Jiao, K. Zhu, and L. Zhang, "Scheduling online EV charging demand response via V2V auctions and local generation," *IEEE Trans. Int. Trans. Syst.*, vol. 23, no. 8, pp. 11436–11452, Aug. 2022.
- [3] O. Nezamuddin, C. L. Nicholas, and E. C. Santos, "The problem of electric vehicle charging: State-of-the-art and an innovative solution," *IEEE Trans. Int. Trans. Syst.*, vol. 23, no. 5, pp. 4663–4673, May 2022.
- [4] C. Liu, H. Liu, G. Cai, S. Cui, H. Liu, and H. Yao, "Novel hybrid LLC resonant and DAB linear DC–DC converter: Average model and experimental verification," *IEEE Trans. Ind. Electron.*, vol. 64, no. 9, pp. 6970–6978, Sep. 2017.
- [5] J. Yong, V. Ramachandaramurthy, K. Tan, and N. Mithulananthan, "A review on the state-of-the-art technologies of electric vehicle, its impacts and prospects," *Renewable Sustain. Energy Rev.*, vol. 49, pp. 365–385, 2015.
- [6] M. G. Egan, D. L. O'Sullivan, J. G. Hayes, M. J. Willers, and C. P. Henze, "Power-factor-corrected single-stage inductive charger for electric vehicle batteries," *IEEE Trans. Ind. Electron.*, vol. 54, no. 2, pp. 1217–1236, Apr. 2007.
- [7] S. Han, S. Han, and K. Sezaki, "Development of an optimal vehicle-to-grid aggregator for frequency regulation," *IEEE Trans. Smart Grid*, vol. 1, no. 1, pp. 65–72, Jun. 2010.
- [8] A. M. A. Haidar and K. M. Muttaqi, "Behavioral characterization of electric vehicle charging loads in a distribution power grid through modeling of battery chargers," *IEEE Trans. Ind. Appl.*, vol. 52, no. 1, pp. 483–492, Jan./Feb. 2016.
- [9] G. Pellegrino, E. Armando, and P. Guglielmi, "An integral battery charger with power factor correction for electric scooter," *IEEE Trans. Power Electron.*, vol. 25, no. 3, pp. 751–759, Mar. 2010.
- [10] B. E. Layton, "A comparison of energy densities of prevalent energy sources in units of joules per cubic meter," *Int. J. Green Energy*, vol. 5, no. 6, pp. 438–455, Dec. 2008.
- [11] M. Chen, A. Mathew, and J. Sun, "Nonlinear current control of single phase PFC converters," *IEEE Trans. Power Electron.*, vol. 18, no. 6, pp. 2187–2194, Nov. 2007.
- [12] B.-K. Lee, J.-P. Kim, S.-G. Kim, and J.-Y. Lee, "An isolated/bidirectional PWM resonant converter for V2G (H) EV on-board charger," *IEEE Trans. Veh. Technol.*, vol. 66, no. 9, pp. 7741–7750, Sep. 2017.
- [13] J. Everts, F. Krismer, J. Van den Keybus, J. Driesen, and J. W. Kolar, "Optimal ZVS modulation of single-phase single-stage bidirectional DAB AC–DC converters," *IEEE Trans. Power Electron.*, vol. 29, no. 8, pp. 3954–3970, Aug. 2014.
- [14] S. Mukherjee, V. R. Chowdhury, P. Shamsi, and M. Ferdowsi, "Model reference adaptive control based estimation of equivalent resistance and reactance in grid-connected inverters," *IEEE Trans. Energy Convers.*, vol. 32, no. 4, pp. 1407–1417, Dec. 2017.
- [15] N. Hou and Y.-W. Li, "Overview and comparison of modulation and control strategies for a non-resonant single-phase dual active bridge DC-DC converter," *IEEE Trans. Power Electron.*, vol. 35, no. 3, pp. 3148–3172, Mar. 2020.
- [16] R. M. Milasi, A. F. Lynch, and Y. W. Li, "Adaptive control of a voltage source converter for power factor correction," *IEEE Trans. Power Electron.*, vol. 28, no. 10, pp. 4767–4779, Oct. 2013.
- [17] K.-P. Huang, Y. Wang, and R.-J. Wai, "Design of power decoupling strategy for single-phase grid-connected inverter under nonideal power grid," *IEEE Trans. Power Electron.*, vol. 34, no. 3, pp. 2938–2955, Mar. 2019.
- [18] A. S. Mir and N. Senroy, "Intelligently controlled flywheel storage for enhanced dynamic performance," *IEEE Trans. Sustain. Energy*, vol. 10, no. 4, pp. 2163–2173, Oct. 2019.
- [19] P. Alemi, C.-J. Bae, and D.-C. Lee, "Resonance suppression based on PR control for single-phase grid-connected inverters with LLCL filters," *IEEE J. Emerg. Sel. Topics Power Electron.*, vol. 4, no. 2, pp. 459–467, Jun. 2016.
- [20] W. Song, Z. Deng, S. Wang, and X. Feng, "A simple model predictive power control strategy for single-phase PWM converters with modulation function optimization," *IEEE Trans. Power Electron.*, vol. 31, no. 7, pp. 5279–5289, Jul. 2016.
- [21] J. Ma, W. Song, S. Wang, and X. Feng, "Model predictive direct power control for single phase three-level rectifier at low switching frequency," *IEEE Trans. Power Electron.*, vol. 33, no. 2, pp. 1050–1062, Feb. 2018.

- [22] H. Wu, S.-C. Wong, C. K. Tse, and Q. Chen, "Control and modulation of bidirectional single-phase AC–DC three-phase-leg SPWM converters with active power decoupling and minimal storage capacitance," *IEEE Trans. Power Electron.*, vol. 31, no. 6, pp. 4226–4240, Jun. 2016.
- [23] L. Schirone, F. Celani, and M. Macellari, "Discrete-time control for DC-AC converters based on sliding mode design," *Inst. Eng. Technol. Power Electron.*, vol. 5, no. 6, pp. 833–840, Jul. 2012.
- [24] R. Guzman, L. G. de Vicuña, J. Morales, M. Castilla, and J. Matas, "Sliding-mode control for a three-phase unity power factor rectifier operating at fixed switching frequency," *IEEE Trans. Power Electron.*, vol. 31, no. 1, pp. 758–769, Jan. 2016.
- [25] N. Vazquez and M. Liserre, "Peak current control and feed-forward compensation of a DAB converter," *IEEE Trans. Ind. Electron.*, vol. 67, no. 10, pp. 8381–8391, Oct. 2020.
- [26] W. Song, N. Hou, and M. Wu, "Virtual direct power control scheme of dual active bridge DC–DC converters for fast dynamic response," *IEEE Trans. Power Electron.*, vol. 33, no. 2, pp. 1750–1759, Feb. 2018.
- [27] F. Krismer and J. W. Kolar, "Closed form solution for minimum conduction loss modulation of DAB converters," *IEEE Trans. Power Electron.*, vol. 27, no. 1, pp. 174–188, Jan. 2012.
- [28] M. C. Kisacikoglu, M. Kesler, and L. M. Tolbert, "Single-phase on-board bidirectional PEV charger for V2G reactive power operation," *IEEE Trans.* Smart Grid, vol. 6, no. 2, pp. 767–775, Mar. 2015.
- [29] B. Singh, S. Kumar, and C. Jain, "Damped-SOGI based control algorithm for solar PV power generating system," *IEEE Trans. Ind. Appl.*, vol. 53, no. 3, pp. 1780–1788, May/Jun. 2017.
- [30] H. K. Khalil, Nonlinear Systems. 3rd ed. Englewood Cliffs, NJ, USA: Prentice-Hall, 2002.
- [31] S. Basu Roy, S. Bhasin, and I. N. Kar, "Robust gradient-based adaptive control of nonlinearly parametrized plants," *IEEE Control Syst. Lett.*, vol. 1, no. 2, pp. 352–357, Oct. 2017.
- [32] D. Mishra, B. Singh, and B. K. Panigrahi, "Modified phase shift control for DAB based bidirectional onboard EV charger," in *Proc. IEEE Int. Conf. Power Electron., Drives Energy Syst.*, 2018, pp. 1–6.
- [33] S. Mohamadian, H. Pairo, and A. Ghasemian, "A straightforward quadrature signal generator for single-phase SOGI-PLL with low susceptibility to grid harmonics," *IEEE Trans. Ind. Electron.*, vol. 69, no. 7, pp. 6997–7007, Jul. 2022.



Debasish Mishra (Student Member, IEEE) received the B. Tech. degree in electrical engineering (with first class and Hons.) from the Biju Patnaik University of Technology, Rourkela, India, and the M.Tech. degree in power electronics from IIT, Varanasi, India, in 2006 and 2012, respectively. From 2012 to 2016, he was an Assistant Professor with ITER, SOA University, Bhubaneswar, India. He is currently working toward the Ph.D. degree with the Department of Electrical Engineering, IIT Delhi, New Delhi. His research interests include design and control of power electronic

converters for electric vehicle applications, power quality enhancement in grid integrated charging stations, and linear and non-linear control applications.



Bhim Singh (Fellow, IEEE) has received the B.E. degree in electrical from the University of Roorkee (Now IIT Roorkee), India, in 1977 and the M.Tech. degree in power apparatus & systems, and the Ph.D. degree in electrical from the IIT Delhi, India, in 1979 and 1983, respectively. In 1983, he was a Lecturer with the Department of Electrical Engineering, University of Roorkee, where he became a Reader in 1988. In December 1990, he joined the Department of Electrical Engineering, IIT Delhi, India, as an Assistant Professor, where he has become an Associate

Professor in 1994 and a Professor in 1997. From 2014 to 2016, he has been the Head of the Department of Electrical Engineering with IIT Delhi. From 2016 to 2019, he has been the Dean, Academics with IIT Delhi. From 2015 to 2021, he has been JC Bose Fellow of DST, Government of India. From 2019 to 2021, he has been CEA Chair Professor. Since July 2021, he has been SERB National Science Chair. Prof. Singh has guided 117 Ph.D. dissertations, and 177 M.E. / M.Tech. /M.S. (R) theses. He has filed 106 patents. He has executed ninety sponsored and consultancy projects. His research interests include solar PV grid interface systems, micro grids, power quality monitoring and mitigation, solar PV water pumping systems, improved power quality AC-DC converters.



Bijaya Ketan Panigrahi (Senior Member, IEEE) received the Ph.D. degree in power systems from Sambalpur University, Sambalpur, India, in 2004. He is currently a Professor with the Department of Electrical Engineering, IIT Delhi, New Delhi, India, where he is also the Head of the Center for Automotive Research and Tribology (CART). His research interests include soft computing, signal processing, power quality, renewable energy systems, power system protection, electric vehicles and charging infrastructure, cyber security of power systems, and the Internet of

Things. Prof. Panigrahi is an Associate Editor for IEEE TRANSACTIONS ON TRANSPORTATION AND ELECTRIFICATION and *IET Smart Grid* and the Editor of *IETE Journal of Research*.